

Posterior Inference for Sparse Hierarchical Non-stationary Models

Karla Monterrubio-Gómez, Lassi Roininen, Sara Wade, Theo Damoulas, and Mark Girolami

Abstract

Gaussian processes are valuable tools for non-parametric modelling, where typically an assumption of stationarity is employed. While removing this assumption can improve prediction, fitting such models is challenging. In this work, hierarchical models are constructed based on Gaussian Markov random fields with stochastic spatially varying parameters. Importantly, this allows for non-stationarity while also addressing the computational burden through a sparse representation of the precision matrix. The prior field is chosen to be Matérn, and two hyperpriors, for the spatially varying parameters, are considered. One hyperprior is Ornstein-Uhlenbeck, formulated through an autoregressive AR(1) process. The other corresponds to the widely used squared exponential. Furthermore, all hyperparameters are treated as unknowns to achieve full uncertainty quantification. In this setting, efficient Markov chain Monte Carlo (MCMC) sampling is challenging due to the strong coupling a posteriori of the parameters and hyperparameters. We develop and compare three MCMC schemes, which are adaptive and therefore free of parameter tuning. An assessment of the ability of the methods to efficiently explore the posterior distribution and to account for non-stationarity is presented. Experiments in both simulated data and a real-world problem of cosmic radio noise are performed. We empirically consider posterior consistency of the estimates with respect to the discretisation scheme and explore the efficiency of the sampling methodologies under different settings.

1 Introduction

Gaussian processes are frequently utilised in constructing powerful nonparametric models, which are appealing due to their analytical properties. The flexibility and nonparametric nature of these models make them appropriate and useful in a wide range of applications. Gaussian process (GP) priors, have been used in geostatistics (Matheron, 1973) under the name of Kriging. They are also common models in other applications; for instance, in atmospheric sciences (Berrocal et al., 2010), medicine (Myllymäki et al., 2014), epidemiology (Xu et al., 2016), biology (Stathopoulos et al., 2014) and inverse problems (Kaipio and Somersalo, 2006).

A large amount of research on Gaussian processes and its applications has focused on models where an assumption of stationarity for the process of interest is made. Nevertheless, this assumption is rarely realistic in practice and as a consequence, several approaches to introduce non-stationarity have been proposed (Sampson et al., 2001; Kim et al., 2005; Anderes and Stein, 2008; Gramacy and Lee, 2012). Although comparative evaluations show that removing the stationary assumption improves predictive accuracy (Gramacy and Lee, 2012; Neto et al., 2014; Fouedjio et al., 2016), fitting such non-stationary models has proven to be challenging. This, combined

with the well-known computational constraints of GP models, arising from storing covariance matrices, solving linear systems and computing determinants, poses important questions on how to efficiently perform Bayesian inference in non-stationary problems.

The stochastic partial differential equation (SPDE) approach introduced by [Lindgren et al. \(2011\)](#) employs Gaussian Markov random fields (GMRFs) to ameliorate the computational burden of working with GP priors and incorporates a non-stationary framework through spatially varying parameters that are modelled as a linear combination of basis functions. Similarly, [Paciorek and Schervish \(2006\)](#) proposed a family of closed-form non-stationary covariance functions with spatially varying parameters modelled by a second latent GP prior. While recognised as a flexible construction, doing inference in a fully Bayesian framework becomes impractical due to the computational demands of such models. Moreover, standard Markov Chain Monte Carlo (MCMC) procedures require careful parameter tuning, exhibit mixing difficulties and require long runs to reach convergence ([Paciorek and Schervish, 2006; Neto et al., 2014](#)).

In this paper, we extend the SPDE formulation of non-stationary GPs considered by [Roininen et al. \(2016\)](#). This model is analogous to SPDE-based constructions in spatial interpolation ([Fuglstad et al., 2015a,b; Yue et al., 2014](#)) and stochastic deep learning ([Paciorek and Schervish, 2006](#)), where the spatially varying parameters are modelled as random objects. We incorporate measurement noise variance and hyperprior parameters as unknowns in the posterior distribution and propose two hyperprior models for the spatially varying length-scale. On one hand, we introduce strong prior smoothness and stationary assumptions through a squared exponential (SE) covariance. On the other hand, we explore an exponential covariance, which when formulated as an autoregressive AR(1) process, provides a sparse representation of the precision matrix.

The hierarchical structure of these models, that we refer to as two-level Gaussian processes, introduces strong dependencies and hence efficient sampling from the posterior distribution of interest is problematic. To address this we introduce and offer a comparative evaluation of three MCMC sampling schemes, which are all free of parameter tuning. The first corresponds to an adaptive Metropolis-within-Gibbs scheme. The second employs Elliptical slice sampling (ELL-SS) combined with re-parametrisations for decoupling the prior, hyperprior, and hyperparameters. The third is a marginal sampler with ELL-SS for a re-parametrised length-scale process. The developed methodology results in a non-stationary hierarchical construction that retains the flexibility of the model introduced by [Paciorek and Schervish \(2006\)](#) but is computationally more efficient, due to the sparsity in the finite-dimensional approximation of the precision matrix. In addition, the inference procedure permits uncertainty quantification of all estimates in the model.

The rest of this paper is organised as follows. We start in Section 2 by summarising related work, providing the connection between the work of [Paciorek and Schervish \(2006\)](#) and the SPDE formulation of GPs ([Lindgren et al., 2011; Roininen et al., 2016](#)). In Section 3, we present the sparse non-stationary hierarchical model and introduce two hyperpriors to model the length-scale. The proposed sampling schemes are detailed in Section 4. Finally, Section 5 presents an empirical evaluation of the proposed methodology, studying the discretisation and sample size effects in one-dimensional non-stationary interpolation problems.

2 Related work and background

2.1 Gaussian Process models

Let us denote by $\mathbf{y} \in \mathbb{R}^m$ noisy realisations of an unknown random process $\{z(\mathbf{x}), \mathbf{x} \in \mathbb{R}^d\}$. A standard Gaussian process regression model assumes

$$y_i = z(\mathbf{x}_i) + \varepsilon_i, \quad (1)$$

where ε_i is zero-mean Gaussian noise with variance σ_ε^2 and $z(\cdot)$ a zero mean Gaussian process. More precisely, the model can be written in a hierarchical form,

$$\begin{aligned} y_i &\sim \mathcal{N}(z(\mathbf{x}_i), \sigma_\varepsilon^2), \quad i = 1, \dots, m, \\ z(\cdot) &\sim \mathcal{GP}(0, C_\phi(\cdot, \cdot)), \\ (\phi, \sigma_\varepsilon^2) &\sim \pi(\phi)\pi(\sigma_\varepsilon^2), \end{aligned} \quad (2)$$

where $C_\phi(\cdot, \cdot)$ is a covariance function, which depends on certain parameters ϕ and must define a valid covariance matrix (symmetric and positive semi-definite). The covariance function encodes important properties of the process, such as its variation and smoothness. Stationary covariance functions only depend on the inputs $(\mathbf{x}_i, \mathbf{x}_j)$ through $|\mathbf{x}_i - \mathbf{x}_j|$ and are most often the default choice. Indeed, the most frequently utilised covariance functions include the stationary squared exponential (SE),

$$C^s(\mathbf{x}_i, \mathbf{x}_j) = \tau^2 \exp\left(-\frac{\|\mathbf{x}_i - \mathbf{x}_j\|^2}{2\lambda^2}\right), \quad (3)$$

and the stationary Matérn family. The latter, recommended by [Stein \(1999\)](#) as the preferred choice, is formulated as

$$C^s(\mathbf{x}_i, \mathbf{x}_j) = \tau^2 \frac{2^{1-\nu}}{\Gamma(\nu)} \left(\frac{\|\mathbf{x}_i - \mathbf{x}_j\|}{\lambda}\right)^\nu K_\nu\left(\frac{\|\mathbf{x}_i - \mathbf{x}_j\|}{\lambda}\right), \quad (4)$$

where $\Gamma(\cdot)$ is the gamma-function, $\nu > 0$ is the smoothness parameter, $\lambda > 0$ is the length-scale, $\tau^2 > 0$ the magnitude or variance parameter, and K_ν denotes the modified Bessel function of the second kind of order ν .

However, the translation-invariance assumption of stationary covariance functions may be inappropriate for certain applications where the process is spatially dependent, such as, for problems in environmental, geospatial and urban sciences. In these cases, a non-stationary formulation of the model is desirable. [Paciorek and Schervish \(2006\)](#) introduced a family of non-stationary covariance functions,

$$C^{\text{NS}}(\mathbf{x}_i, \mathbf{x}_j) = \frac{\tau^2 |\Sigma(\mathbf{x}_i)|^{\frac{1}{4}} |\Sigma(\mathbf{x}_j)|^{\frac{1}{4}}}{|(\Sigma(\mathbf{x}_i) + \Sigma(\mathbf{x}_j))/2|^{\frac{1}{2}}} R\left(\sqrt{Q_{ij}}\right),$$

where $R(\cdot)$ is a stationary correlation function on \mathbb{R} ; $\Sigma(\cdot)$ is a $d \times d$ spatially varying covariance matrix, referred to as a kernel matrix, which describes local anisotropies; and

$$Q_{ij} = (\mathbf{x}_i - \mathbf{x}_j)^T ((\Sigma(\mathbf{x}_i) + \Sigma(\mathbf{x}_j))/2)^{-1} (\mathbf{x}_i - \mathbf{x}_j).$$

We note that for one-dimensional problems, the kernel matrices, $\Sigma(\cdot)$, are reduced to scalars, which we denote as $\ell(\cdot)$. The non-stationary version of the Matérn covariance function is therefore,

$$C^{\text{NS}}(\mathbf{x}_i, \mathbf{x}_j) = \frac{\tau^2 |\Sigma(\mathbf{x}_i)|^{\frac{1}{4}} |\Sigma(\mathbf{x}_j)|^{\frac{1}{4}}}{\Gamma(\nu) 2^{\nu-1} |(\Sigma(\mathbf{x}_i) + \Sigma(\mathbf{x}_j))/2|^{\frac{1}{2}}} \left(2\sqrt{\nu Q_{ij}}\right)^\nu K_\nu\left(2\sqrt{\nu Q_{ij}}\right), \quad (5)$$

with hyperparameters $\phi = \{\Sigma(\cdot), \nu, \tau^2\}$. When employing this type of non-stationary covariance functions in equation (2), we are required to infer the kernel matrices at every location where the process was observed. [Paciorek and Schervish \(2006\)](#) modelled the kernel matrices as a continuous-parameter random process by utilising its spectral decomposition. Nonetheless, this approach results in a computationally expensive inference procedure ([Paciorek and Schervish, 2006](#), Section 5.1) even for one-dimensional problems. As a consequence, alternative approaches to model the spatially varying parameters have been proposed in the literature ([Risser, 2016](#); [Neto et al., 2014](#); [Lang et al., 2007](#)).

In one-dimensional settings, when modelling the spatially varying length-scale with a GP, the hierarchical formulation of the model is

$$\begin{aligned} y_i &\sim \mathcal{N}(z(x_i), \sigma_\varepsilon^2), \quad i = 1, \dots, m, \\ z(\cdot) &\sim \mathcal{GP}(0, C_\phi^{\text{NS}}(\cdot, \cdot)), \\ \log \ell(\cdot) &\sim \mathcal{GP}(0, C_\varphi^{\text{S}}(\cdot, \cdot)), \\ (\tau^2, \varphi, \sigma_\varepsilon^2) &\sim \pi(\tau^2)\pi(\varphi)\pi(\sigma_\varepsilon^2), \end{aligned} \tag{6}$$

where $C_\phi^{\text{NS}}(\cdot, \cdot)$ is as in equation (5), and $C_\varphi^{\text{S}}(\cdot, \cdot)$ corresponds to a stationary covariance function with parameters φ . Note that the prior for the spatially varying length-scale is assigned over a transformed parameter, and for notational simplicity, we define $u(\cdot) := \log \ell(\cdot)$. Performing inference under this model amounts to exploring the posterior:

$$\pi(\mathbf{z}, \mathbf{u}, \tau^2, \varphi, \sigma_\varepsilon^2 \mid \mathbf{y}) \propto \mathcal{N}(\mathbf{y} \mid \mathbf{z}, \sigma_\varepsilon^2 I_m) \mathcal{N}(\mathbf{z} \mid 0, C_\phi^{\text{NS}}) \mathcal{N}(\mathbf{u} \mid 0, C_\varphi^{\text{S}}) \pi(\tau^2) \pi(\varphi) \pi(\sigma_\varepsilon^2), \tag{7}$$

where $\mathbf{z} \in \mathbb{R}^m$ denotes the vector formed by the latent process at the observed locations, and $\mathbf{u} \in \mathbb{R}^m$ denotes the vector of transformed spatially varying length-scales.

Efficient sampling from the posterior in equation (7) is challenging and the computational burden introduced by the spatially varying parameter is even noticeable in one-dimensional problems ([Paciorek and Schervish, 2006](#); [Heinonen et al., 2016](#)). These difficulties arise from different sources. First, the computational complexity inherited from working dense covariance matrices makes the model unsuitable for large datasets. Second, the latent processes and hyperparameters tend to be strongly coupled a posteriori, which leaves vanilla MCMC procedures inefficient. Finally, as in a stationary formulation, the model is sensitive to the choice of hyperparameters, φ , and therefore these must be inferred ([Neto et al., 2014](#)).

2.2 SPDE formulation of Matérn fields

[Lindgren et al. \(2011\)](#) showed that Gaussian Markov random fields can be presented equivalently as stochastic partial differential equations. By fixing $\nu = 2 - d/2$, a GP with stationary Matérn covariance (4) can be defined ([Lindgren et al., 2011](#); [Roininen et al., 2014](#)) through

$$(1 - \lambda^2 \Delta) z = \tau \sqrt{\lambda^d} w, \tag{8}$$

where $\Delta := \sum_{k=1}^d \frac{\partial^2}{\partial x_k^2}$ is the Laplace operator, w is white noise on \mathbb{R}^d , and we choose

$$\text{Var}(w) = \frac{\Gamma(\nu + d/2)(4\pi)^{d/2}}{\Gamma(\nu)}.$$

Analogous to the construction of [Paciorek and Schervish \(2006\)](#) for non-stationary covariance functions with spatially varying length-scales, [Roininen et al. \(2016\)](#) derive a stochastic partial

differential equation formulation for non-stationary Matérn fields,

$$(1 - \ell(\cdot)^2 \Delta) z = \tau \sqrt{\ell(\cdot)^d} w, \quad (9)$$

where $\ell(\cdot)$ is a spatially varying length-scale, that is modelled as a log-transformed continuous-parameter GP model in the hyperprior in equation (6). An alternative formulation was proposed by [Lindgren et al. \(2011, Section 3.2\)](#), where spatially varying parameters were modelled through a basis function representation. Such a choice gives computational advantages, as the parameter space is lower than when using GP hyperpriors. However, this requires selecting the number of basis functions, and the ability to flexibly recover changes in the length-scale strongly depends on this choice. A finite-dimensional approximation of our continuous-parameter model (9), as well as the [Lindgren et al. \(2011\)](#) model, can be written in vector-matrix format as:

$$L(\ell) \mathbf{z} = \mathbf{w}, \quad (10)$$

where $L(\ell)$ is a sparse matrix depending on $\ell_j := \ell(jh)$, with h denoting the discretisation step in a chosen finite difference approximation. This model is constructed in such a way that the finite-dimensional approximation (10) converges to the continuous-parameter model (9) in the discretisation limit $h \rightarrow 0$ (for proofs, see [Roininen et al. \(2016\)](#)). This property guarantees that irrespective of the choice of h , the posteriors, and hence also the estimators, on different meshes, that are dense enough, are essentially the same.

Employing a GP to model $\ell(\cdot)$ results in a similar construction to that discussed in Section 2.1. In the next sections, we extend the work of [Roininen et al. \(2016\)](#), by including inference of the measurement noise variance and the length-scale hyperparameter. Additionally, we explore different hyperprior models and discuss MCMC algorithms to do inference with these types of models.

3 Sparse non-stationary hierarchical models

The Gaussian process formulation in equation (1) can be rephrased through

$$\mathbf{y} = \mathcal{A}z + \boldsymbol{\varepsilon}, \quad (11)$$

where \mathcal{A} represents a linear mapping from some function space to a finite-dimensional space \mathbb{R}^m , and where $\boldsymbol{\varepsilon} \in \mathbb{R}^m$ is assumed to be zero-mean Gaussian noise with variance $\sigma_\varepsilon^2 I_m$, which is independent of z . For computational reasons, we discretise equation (11), such that $\mathcal{A}z \approx A\mathbf{z}$, obtaining,

$$\mathbf{y} = A\mathbf{z} + \boldsymbol{\varepsilon},$$

where $A \in \mathbb{R}^{m \times n}$ is a known matrix and $\mathbf{z} \in \mathbb{R}^n$ with $\mathbf{z} \sim \mathcal{N}(0, C_\phi^{\text{NS}})$. Our aim is to decompose the inverse prior covariance $C_\phi^{\text{NS}^{-1}} := Q_\phi = L(\phi)^T L(\phi)$, where $L(\phi)$ is a sparse matrix that depends on parameters ϕ . The required decomposition can be achieved employing the stochastic partial differential equation approach from Section 2.2 through equation (10).

Below, we give the explicit hierarchical formulation of the model,

$$\begin{aligned} \mathbf{y} \mid \mathbf{z}, \sigma_\varepsilon^2 &\sim \mathcal{N}(A\mathbf{z}, \sigma_\varepsilon^2 I_m), \\ \mathbf{z} \mid \phi &\sim \mathcal{N}(0, Q_\phi^{-1}) \\ \mathbf{u} \mid \boldsymbol{\varphi} &\sim \mathcal{N}(0, C_\phi) \\ (\tau^2, \sigma_\varepsilon^2, \boldsymbol{\varphi}) &\sim \pi(\tau^2) \pi(\sigma_\varepsilon^2) \pi(\boldsymbol{\varphi}), \end{aligned} \quad (12)$$

where the key component of the model is Q_ϕ , the inverse covariance of the Gaussian Markov random field employed to represent the non-stationary Gaussian process. This precision matrix depends on \mathbf{u} and τ^2 . In particular, \mathbf{u} is assumed to be a zero-mean Gaussian process that describes the spatially varying length-scale, and φ denotes the parameters of the covariance function that describe the properties of the length-scales, such as its smoothness, and to which we also assign prior distributions. A plate diagram of this model is given in Figure 1(left).

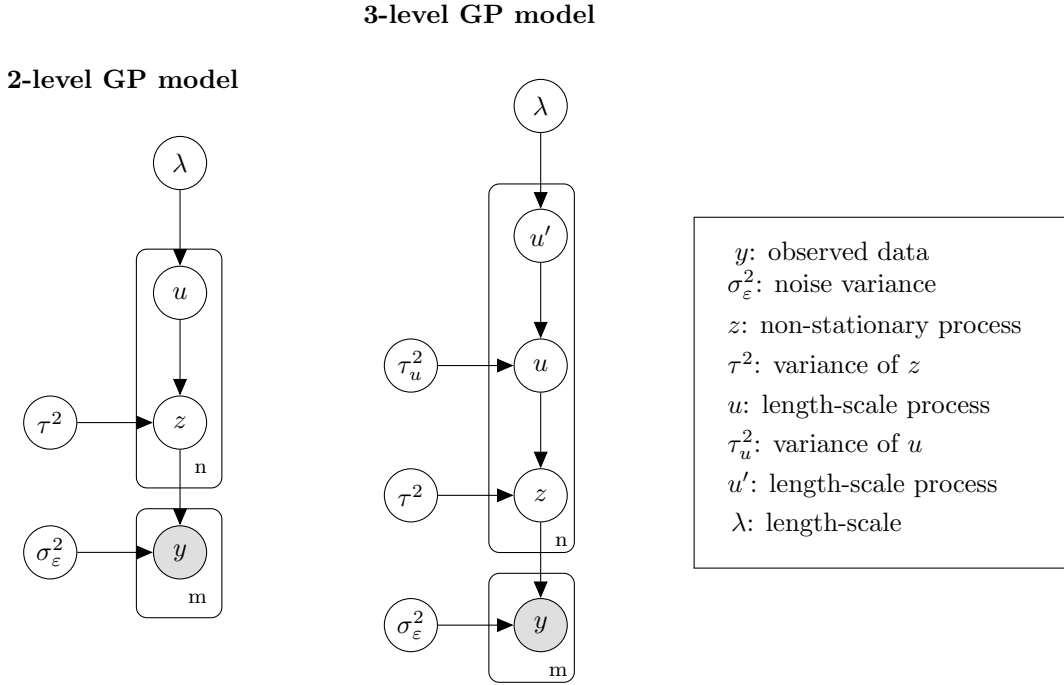


Figure 1: Plate diagram for a non-stationary hierarchical model.

In the following sections, we discuss different types of hyperpriors for \mathbf{u} . Notice that we are free to assign an inhomogeneous Matérn field for the length-scale process, introducing more flexibility to the model. A graphical representation of this type of construction is given to the right of Figure 1. For simplicity, we focus our analysis on the simplest case, when the parameters of the length-scale process are restricted to be constant along the input space. In addition, for both stationary and non-stationary covariance functions, the length-scale and magnitude parameters cannot be estimated consistently (Zhang, 2004), and for this reason, it is common to fix one of them or to employ a re-parametrisation. Here we set the magnitude parameter of both processes in the model to one. Consequently, the posterior of interest is simplified to

$$\pi(\mathbf{z}, \mathbf{u}, \lambda, \sigma_\varepsilon^2 \mid \mathbf{y}) \propto \mathcal{N}(\mathbf{y} \mid A\mathbf{z}, \sigma_\varepsilon^2 I_m) \mathcal{N}(\mathbf{z} \mid 0, Q_\mathbf{u}^{-1}) \mathcal{N}(\mathbf{u} \mid 0, C_\lambda) \pi(\lambda) \pi(\sigma_\varepsilon^2). \quad (13)$$

Notice that compared to the posterior shown in equation (7), the likelihood function in (13) is different, and we employ the inverse covariance of the GMRF in equation (9) to make computationally efficient inference. In addition, although \mathbf{z} can be marginalised analytically, resulting in the posterior

$$\pi(\mathbf{u}, \lambda, \sigma_\varepsilon^2 \mid \mathbf{y}) \propto \mathcal{N}(\mathbf{y} \mid 0, A Q_\mathbf{u}^{-1} A^\top + \sigma_\varepsilon^2 I_m) \mathcal{N}(\mathbf{u} \mid 0, C_\lambda) \pi(\lambda) \pi(\sigma_\varepsilon^2), \quad (14)$$

employing (13) is more appealing as we can take direct advantage of the sparse structure in the

precision matrix. In contrast, the precision matrix of the marginal likelihood in (14) corresponds to a dense matrix.

The proposed approach considers full-scale uncertainty quantification of all the estimates, where all the processes and parameters are modelled as random objects, building on and further developing the work by [Roininen et al. \(2016\)](#). Furthermore, through the matrix A , we are able to define the grid resolution of the latent fields. In particular, for more rough processes, we may be interested in finer resolutions, while for smooth functions, a sparse grid may be sufficient to obtain an accurate representation. In Section 4, we discuss MCMC techniques to do inference in these types of models.

3.1 AR(1) hyperprior

It would be tempting to use any stochastic process as a hyperprior for the length-scale ℓ . However, in [Roininen et al. \(2016\)](#), it was shown that something smoother than white noise is needed, otherwise different discretisations of z may affect the posterior estimates. When the smoothness parameter of the stationary Matérn covariance (equation (4)) is set to $\nu = 1/2$, we have an exponential covariance function,

$$C^s(x_i, x_j) = \tau^2 \exp\left(-\frac{|x_i - x_j|}{\lambda}\right).$$

This is the Ornstein-Uhlenbeck covariance, and it is well-known to have non-differentiable sample paths. Employing this covariance function in place of C_φ in the model (12) allows quick changes in its behaviour, while at the same time, it is smoother than white noise.

The Ornstein-Uhlenbeck process is the continuous-time counterpart of the first-order autoregressive model AR(1) given by

$$u_j = \beta u_{j-1} + e_j, \quad e_j \sim \mathcal{N}(0, \sigma^2),$$

where u is the object of interest and u_j is on an uniform lattice $t_j := jh$, $j \in \mathbb{Z}$ with discretisation step h . Without a proof, we note that the AR(1) has an exponential autocovariance for all $\beta > 0$ except for $\beta = 1$ which corresponds to Gaussian random walk, i.e. Brownian motion. We note that the stable AR(1) requires that $\beta < 1$, but here, as our goal is in forming covariance matrices, this is not a necessary condition.

Let us denote by $a_0 := 1/\sigma$ and $a_1 := \beta/\sigma$. Then we can construct the inverse of the exponential covariance matrix $C_\lambda^{s-1} := Q_\lambda = L(\lambda)^T L(\lambda)$, where $L(\lambda)$ is a sparse matrix that depends on λ . More precisely,

$$L(\lambda) = \begin{pmatrix} a_0 & a_1 & & & \\ & a_0 & a_1 & & \\ & & \ddots & \ddots & \\ & & & a_0 & a_1 \\ & & & & 1 \end{pmatrix}, \quad (15)$$

where the coefficients a_0 and a_1 are defined as

$$a_0 = \left(\sqrt{\frac{h}{\lambda}} + \sqrt{\frac{h}{\lambda} + 4\frac{\lambda}{h}} \right) / \sqrt{8}, \quad a_1 = \left(\sqrt{\frac{h}{\lambda}} - \sqrt{\frac{h}{\lambda} + 4\frac{\lambda}{h}} \right) / \sqrt{8}.$$

Hence, we have a sparse representation for the hyperprior precision matrix. The posterior distribution in equation (13) can therefore be rewritten as

$$\pi(\mathbf{z}, \mathbf{u}, \lambda, \sigma_\varepsilon^2 \mid \mathbf{y}) \propto \mathcal{N}(\mathbf{y} \mid A\mathbf{z}, \sigma_\varepsilon^2 I_m) \mathcal{N}(\mathbf{z} \mid 0, Q_{\mathbf{u}}^{-1}) \mathcal{N}(\mathbf{u} \mid 0, Q_\lambda^{-1}) \pi(\lambda) \pi(\sigma_\varepsilon^2), \quad (16)$$

where we use the sparse precision matrix to model the varying length-scale process.

3.2 Squared exponential hyperprior

In contrast to the AR(1) hyperprior, we have the squared exponential (SE) hyperprior, which is obtained when we use equation (3) in place of C_φ in the model from equation (12). This covariance function, also referred to as the radial basis function (RBF), is recovered when $\nu \rightarrow \infty$ in the stationary Matérn covariance from equation (4). Sample paths from a SE are infinitely differentiable and consequently very smooth. Therefore, when employing a SE hyperprior for the length-scale process, we introduce strong prior smoothness assumptions on how the correlation of the non-stationary process changes with distance. We note that for the SE hyperprior, the precision matrix is dense, as we cannot use the autoregressive formulation of Section 3.1. Therefore, the posterior distribution, in this case, corresponds to that shown in equation (13).

4 Algorithms

In order to draw samples from the posterior distributions of interest, we propose three MCMC sampling approaches. The first draws samples from the multidimensional vector \mathbf{u} through an adaptive Metropolis-within-Gibbs algorithm. The second employs ancillary augmentation (Yu and Meng, 2011) over \mathbf{z} and \mathbf{u} and uses elliptical slice sampling (ELL-SS) (Murray et al., 2010) over the re-parametrised length-scale process. The third integrates out the non-stationary process, resulting in a marginal sampler that draws from \mathbf{u} by combining ancillary augmentation and ELL-SS to break the correlation between \mathbf{u} and λ .

4.1 Metropolis-within-Gibbs (MWG)

This sampling scheme is inspired by that proposed in Roininen et al. (2016) and additionally incorporates adaptive random walks for the noise variance and length-scale hyperparameter. Furthermore, we incorporate adaptation (Roberts and Rosenthal, 2009) for the length-scale process in order to obtain a Metropolis-within-Gibbs (MWG) scheme that is free of parameter tuning. The generic procedure is detailed in Algorithm 1.

Regardless of the hyperprior employed in the model, MWG offers computational gains due to the fact that we are not required to invert matrices to evaluate the log prior density of \mathbf{z} ,

$$\log \pi(\mathbf{z} \mid \mathbf{u}) = -\frac{n}{2} \log(2\pi) + \log \det(L(\mathbf{u})) - \frac{1}{2} \mathbf{z}^\top L(\mathbf{u})^\top L(\mathbf{u}) \mathbf{z}.$$

Instead, we can reconstruct the inverse covariance through $C_{\mathbf{u}}^{\text{NS}-1} = L(\mathbf{u})^\top L(\mathbf{u})$. Moreover, the normalisation constant includes a log-determinant computation, which can be numerically unstable and computationally expensive. Employing a single-component Metropolis-Hastings algorithm simplifies this operation; for details, see Roininen et al. (2016, Section 6).

Algorithm 1 Metropolis-within-Gibbs (MWG)

Require: A , $\sigma_\varepsilon^{2(0)}$, $\mathbf{u}^{(0)}$, $\mathbf{z}^{(0)}$ and $\lambda^{(0)}$

1: **for** $t = 1$ to T **do**

2: Draw: $\log \sigma_\varepsilon^2 | \log \sigma_\varepsilon^{2(t-1)} \sim \mathcal{N}(\log \sigma_\varepsilon^{2(t-1)}, s_1)$

3: Compute: $\alpha_{\sigma_\varepsilon^2} = \min \left\{ 1, \frac{\mathcal{N}(\mathbf{y} | A\mathbf{z}^{(t-1)}, \sigma_\varepsilon^2 I_m) \pi(\log \sigma_\varepsilon^2)}{\mathcal{N}(\mathbf{y} | A\mathbf{z}^{(t-1)}, \sigma_\varepsilon^{2(t-1)} I_m) \pi(\log \sigma_\varepsilon^{2(t-1)})} \right\}$

4: With probability $\alpha_{\sigma_\varepsilon^2}$ set $\log \sigma_\varepsilon^{2(t)} = \log \sigma_\varepsilon^2$, otherwise set $\log \sigma_\varepsilon^{2(t)} = \log \sigma_\varepsilon^{2(t-1)}$

5: Run Adaptation for s_1

6: Draw: $\boldsymbol{\eta} \sim \mathcal{N}(0, I_{m+n})$

7: Set: $\mathbf{z}^{(t)} = \begin{pmatrix} \sigma_\varepsilon^{-1(t)} A \\ L(\mathbf{u}^{(t-1)}) \end{pmatrix}^\dagger \left(\begin{pmatrix} \sigma_\varepsilon^{-1(t)} \mathbf{y} \\ 0 \end{pmatrix} + \boldsymbol{\eta} \right)$ $\triangleright \dagger$ denotes the matrix pseudoinverse

8: Draw: $\mathbf{u} \sim \mathcal{N}(\mathbf{u}^{(t-1)}, P)$ $\triangleright P = \text{diag}(\sigma_{u_1}^2, \dots, \sigma_{u_n}^2)$

9: Set: $\mathbf{u}' = \mathbf{u}^{(t-1)}$ and $\mathbf{u}^{(t)} = \mathbf{u}^{(t-1)}$

10: **for** $k = 1$ to n **do**

11: Set: $\mathbf{u}_{j \neq k} = (u_1^{(t)}, \dots, u_{k-1}^{(t)}, u_k, u_{k+1}^{(t-1)}, \dots, u_n^{(t-1)})^T$

12: Compute: $\alpha_{u_k} = \min \left\{ 1, \frac{\mathcal{N}(\mathbf{z}^{(t)} | 0, C_{\mathbf{u}_{j \neq k}}) \mathcal{N}(\mathbf{u}_{j \neq k} | 0, C_\lambda^{(t-1)})}{\mathcal{N}(\mathbf{z}^{(t)} | 0, C_{\mathbf{u}'}) \mathcal{N}(\mathbf{u}' | 0, C_\lambda^{(t-1)})} \right\}$

13: With probability α_{u_k} set $u_k^{(t)} = u_k$ and $u'_k = u_k$; otherwise set $u_k^{(t)} = u_k^{(t-1)}$

14: **end for**

15: Run Adaptation for P

16: Draw: $\log \lambda | \log \lambda^{(t-1)} \sim \mathcal{N}(\log \lambda^{(t-1)}, s_2)$

17: Compute: $\alpha_\lambda = \min \left\{ 1, \frac{\mathcal{N}(\mathbf{u}^{(t)} | 0, C_\lambda) \pi(\log \lambda)}{\mathcal{N}(\mathbf{u}^{(t)} | 0, C_{\lambda^{(t-1)}}) \pi(\log \lambda^{(t-1)})} \right\}$

18: With probability α_λ set $\log \lambda^{(t)} = \log \lambda$, otherwise set $\log \lambda^{(t)} = \log \lambda^{(t-1)}$

19: Run Adaptation for s_2

20: **end for**

Further computational gains are possible when we utilise the AR(1) hyperprior. Similar to the prior density of \mathbf{z} , we can evaluate the log prior density of \mathbf{u} through

$$\log \pi(\mathbf{u} | \lambda) = -\frac{n}{2} \log(2\pi) + \log \det(L(\lambda)) - \frac{1}{2} \mathbf{u}^T L(\lambda)^T L(\lambda) \mathbf{u}.$$

However, this is not possible when utilising SE hyperprior. In that case, we require the inversion of an $n \times n$ matrix. The log prior density is evaluated as

$$\log \pi(\mathbf{u} | \lambda) = -\frac{n}{2} \log(2\pi) - \frac{1}{2} \log \det(C_\lambda) - \frac{1}{2} \mathbf{u}^T C_\lambda^{-1} \mathbf{u}.$$

Our simulation studies show that this algorithm can perform badly when the hyperprior for $u(\cdot)$ has strong smoothness assumptions, such as those induced by employing a SE covariance function. This flaw motivates us to explore elliptical slice sampling, a state-of-the-art MCMC algorithm for latent Gaussian models (Murray et al., 2010).

4.2 Whitened Elliptical Slice Sampling (w-ELL-SS)

Elliptical slice sampling is known to perform well with Gaussian priors that are strongly coupled (Murray et al., 2010). Here, we combine this sampling algorithm with ancillary augmentation or *whitening* (Yu and Meng, 2011), which represents a computationally cheap and effective strategy to break the correlation between the prior and its corresponding hyperparameters (Filippone et al., 2013; Murray and Adams, 2010).

We define $\mathbf{z} = L(\mathbf{u})^{-1} \boldsymbol{\xi}$ with $\boldsymbol{\xi} \sim \mathcal{N}(0, I_n)$, and $\mathbf{u} = R_\lambda \boldsymbol{\zeta}$ with $\boldsymbol{\zeta} \sim \mathcal{N}(0, I_n)$. For the AR(1) hyperprior, $R_\lambda := L(\lambda)^{-1}$, with $L(\lambda)$ as in equation (15); whereas, for the SE hyperprior, we define R_λ to be the lower-triangular Cholesky factor of C_λ , such that $C_\lambda = R_\lambda R_\lambda^T$. Applying whitening for both \mathbf{z} and \mathbf{u} results in the joint posterior

$$p(\boldsymbol{\zeta}, \boldsymbol{\xi}, \lambda, \sigma_\varepsilon^2 | \mathbf{y}) \propto \mathcal{N}(\mathbf{y} | AL(R_\lambda \boldsymbol{\zeta})^{-1} \boldsymbol{\xi}, \sigma_\varepsilon^2 I_m) \mathcal{N}(\boldsymbol{\xi} | 0, I_n) \mathcal{N}(\boldsymbol{\zeta} | 0, I_n) \pi(\lambda) \pi(\sigma_\varepsilon^2).$$

This sampling scheme does not require dense matrix inversions nor expensive log determinant computations. However, as ELL-SS is a rejection free sampling method, each iteration may require several likelihood evaluations. We further note whitening requires the evaluation of (a decomposition of) the covariance matrix, not the precision matrix, which minimizes the computational gains of employing the AR hyperprior over the SE hyperprior. Specifically, on one hand, we need to invert a sparse matrix for the AR hyperprior, and on the other hand, we need a Cholesky decomposition of a dense matrix for the SE hyperprior. The sampling method is described in Algorithm 2.

4.3 Marginal Elliptical Slice Sampling (m-ELL-SS)

In simulation studies, we found that integrating out the latent variables \mathbf{z} significantly improves the mixing of the chains for \mathbf{u} and its hyperparameters. The log marginal likelihood of the data corresponds to

$$\log p(\mathbf{y} | \mathbf{u}, \lambda, \sigma_\varepsilon^2) = -\frac{m}{2} \log(2\pi) - \frac{1}{2} \log \det(\Psi) - \frac{1}{2} \mathbf{y}^T \Psi^{-1} \mathbf{y},$$

where $\Psi = A Q_{\mathbf{u}}^{-1} A^T + \sigma_\varepsilon^2 I_m$. Similar to w-ELL-SS, from Section 4.2, we use whitening to de-couple \mathbf{u} and λ . The re-parametrisation corresponds again to $\mathbf{u} = R_\lambda \boldsymbol{\zeta}$ where $\boldsymbol{\zeta} \sim \mathcal{N}(0, I_n)$, and

Algorithm 2 Whitened Elliptical Slice Sampling (w-ELL-SS)

Require: A , $\sigma_\varepsilon^{2(0)}$, $\zeta^{(0)}$, $\xi^{(0)}$ and $\lambda^{(0)}$

```

1: for  $t = 1$  to  $T$  do
2:   Compute:  $\mathbf{u} = R_{\lambda^{(t-1)}} \zeta^{(t-1)}$ 
3:   Compute:  $\mathbf{z} = L(\mathbf{u})^{-1} \xi^{(t-1)}$ 
4:   Draw:  $\log \sigma_\varepsilon^2 \mid \log \sigma_\varepsilon^{2(t-1)} \sim \mathcal{N}(\log \sigma_\varepsilon^{2(t-1)}, s_1)$ 
5:   Compute:  $\alpha_{\sigma_\varepsilon^2} = \min \left\{ 1, \frac{\mathcal{N}(\mathbf{y} \mid A\mathbf{z}, \sigma_\varepsilon^2 I_m) \pi(\log \sigma_\varepsilon^2)}{\mathcal{N}(\mathbf{y} \mid A\mathbf{z}, \sigma_\varepsilon^{2(t-1)} I_m) \pi(\log \sigma_\varepsilon^{2(t-1)})} \right\}$ 
6:   With probability  $\alpha_{\sigma_\varepsilon^2}$  set  $\log \sigma_\varepsilon^{2(t)} = \log \sigma_\varepsilon^2$ , otherwise set  $\log \sigma_\varepsilon^{2(t)} = \log \sigma_\varepsilon^{2(t-1)}$ 
7:   Run Adaptation for  $s_1$ 
8:   Draw:  $\nu \sim \mathcal{N}(0, I_m)$ 
9:   Draw:  $\beta \sim \mathcal{U}[0, 1]$ 
10:  Compute:  $\kappa = \log \mathcal{N}(\mathbf{y} \mid A\mathbf{z}, \sigma_\varepsilon^{2(t)} I_m) + \log \beta$ 
11:  Draw:  $\theta \sim \mathcal{U}[0, 2\pi]$ 
12:  Define:  $[\theta_{\min}, \theta_{\max}] = [\theta - 2\pi, \theta]$ 
13:  Propose:  $\zeta' = \zeta^{(t-1)} \cos \theta + \nu \sin \theta$ 
14:  Update:  $\mathbf{u} = R_{\lambda^{(t-1)}} \zeta'$ 
15:  Update:  $\mathbf{z} = L(\mathbf{u})^{-1} \xi^{(t-1)}$ 
16:  if  $\log \mathcal{N}(\mathbf{y} \mid A\mathbf{z}, \sigma_\varepsilon^{2(t)} I_m) > \kappa$  then
17:    Set:  $\zeta^{(t)} = \zeta'$ 
18:  else
19:    if  $\theta < 0$  then
20:       $\theta_{\min} = \theta$ 
21:    else
22:       $\theta_{\max} = \theta$ 
23:    end if
24:    Draw:  $\theta \sim \mathcal{U}[\theta_{\min}, \theta_{\max}]$ 
25:    Go back to step 13.
26:  end if
27:  Draw:  $\log \lambda \mid \log \lambda^{(t-1)} \sim \mathcal{N}(\log \lambda^{(t-1)}, s_2)$ 
28:  Compute:  $\mathbf{u}' = R_\lambda \zeta^{(t)}$ 
29:  Compute:  $\mathbf{z}' = L(\mathbf{u}') \xi^{(t-1)}$ 
30:  Compute:  $\alpha_\lambda = \min \left\{ 1, \frac{\mathcal{N}(\mathbf{y} \mid A\mathbf{z}', \sigma_\varepsilon^{2(t)} I_m) \pi(\log \lambda)}{\mathcal{N}(\mathbf{y} \mid A\mathbf{z}, \sigma_\varepsilon^{2(t)} I_m) \pi(\log \lambda^{(t-1)})} \right\}$ 
31:  With probability  $\alpha_\lambda$  set  $\log \lambda^{(t)} = \log \lambda$ , and  $\mathbf{u} = \mathbf{u}'$ ; otherwise, set  $\log \lambda^{(t)} = \log \lambda^{(t-1)}$ 
32:  Draw:  $\eta \sim \mathcal{N}(0, I_{m+n})$ 
33:  Set:  $\xi^{(t)} = \begin{pmatrix} \sigma_\varepsilon^{-1(t)} A L(\mathbf{u})^{-1} \\ I_n \end{pmatrix}^\dagger \left( \begin{pmatrix} \sigma_\varepsilon^{-1(t)} \mathbf{y} \\ 0 \end{pmatrix} + \eta \right)$   $\triangleright \dagger$  denotes the matrix pseudoinverse
34: end for

```

$R_\lambda := L(\lambda)^{-1}$ for the AR(1) hyperprior, or $R_\lambda := \text{chol}(C_\lambda)$ for the SE hyperprior. The posterior distribution is therefore,

$$p(\zeta, \lambda, \sigma_\varepsilon^2 \mid \mathbf{y}) \propto \mathcal{N}(\mathbf{y} \mid 0, A Q_{\zeta, \lambda}^{-1} A^T + \sigma_\varepsilon^2 I_n) \mathcal{N}(\zeta \mid 0, I_m) \pi(\lambda) \pi(\sigma_\varepsilon^2).$$

It is important to emphasize that employing the marginal likelihood brings in extra computational cost, as the calculation of $\log \det(\Psi)$ can not be simplified. However, notice also that the inversion of Ψ can be computed employing the Woodbury identity; such that, $\Psi^{-1} = \sigma_\varepsilon^{-2} I_m - \sigma_\varepsilon^{-2} A (L(\mathbf{u})^T L(\mathbf{u}) + \sigma_\varepsilon^{-2} A^T A)^{-1} A^T$. This results in the inversion of a sparse matrix rather than an inversion of a dense matrix Ψ . In addition, in contrast to MWG, this scheme performs well regardless of the hyperprior employed. Again, we note that as is the case for the w-ELL-SS in Section 4.2, whitening mitigates the computational gains of utilising an AR hyperprior over the SE hyperprior. The sampling scheme is detailed in Algorithm 3.

Algorithm 3 Marginal Elliptical Slice Sampling (m-ELL-SS)

Require: $A, \sigma_\varepsilon^{2(0)}, \zeta^{(0)}, \lambda^{(0)}$, and $\mathbf{u} = R_{\lambda^{(0)}} \zeta^{(0)}$

1: **for** $t = 1$ to T **do**

2: Draw: $\log \sigma_\varepsilon^{2(t-1)} \sim \mathcal{N}(\log \sigma_\varepsilon^{2(t-1)}, s_1)$

3: Compute: $\alpha_{\sigma_\varepsilon^2} = \min \left\{ 1, \frac{\mathcal{N}(\mathbf{y} \mid 0, A Q_{\mathbf{u}}^{-1} A^T + \sigma_\varepsilon^{2(t-1)} I_m) \pi(\log \sigma_\varepsilon^{2(t-1)})}{\mathcal{N}(\mathbf{y} \mid 0, A Q_{\mathbf{u}}^{-1} A^T + \sigma_\varepsilon^{2(t-1)} I_m) \pi(\log \sigma_\varepsilon^{2(t-1)})} \right\}$

4: With probability $\alpha_{\sigma_\varepsilon^2}$ set $\log \sigma_\varepsilon^{2(t)} = \log \sigma_\varepsilon^{2(t-1)}$, otherwise set $\log \sigma_\varepsilon^{2(t)} = \log \sigma_\varepsilon^{2(t-1)}$

5: Run Adaptation for s_1

6: Draw: $\boldsymbol{\nu} \sim \mathcal{N}(0, I_m)$

7: Draw: $\beta \sim \mathcal{U}[0, 1]$

8: Compute: $\kappa = \log \mathcal{N}(\mathbf{y} \mid 0, A Q_{\mathbf{u}}^{-1} A^T + \sigma_\varepsilon^{2(t)} I_m) + \log \beta$

9: Draw: $\theta \sim \mathcal{U}[0, 2\pi]$

10: Define: $[\theta_{\min}, \theta_{\max}] = [\theta - 2\pi, \theta]$

11: Propose: $\zeta' = \zeta^{(t-1)} \cos \theta + \boldsymbol{\nu} \sin \theta$

12: Compute: $\mathbf{u} = R_{\lambda^{(t-1)}} \zeta'$

13: **if** $\log \mathcal{N}(\mathbf{y} \mid 0, A Q_{\mathbf{u}}^{-1} A^T + \sigma_\varepsilon^{2(t)} I_m) > \kappa$ **then**

14: Set: $\zeta^{(t)} = \zeta'$

15: **else**

16: **if** $\theta < 0$ **then**

17: $\theta_{\min} = \theta$

18: **else**

19: $\theta_{\max} = \theta$

20: **end if**

21: Draw: $\theta \sim \mathcal{U}[\theta_{\min}, \theta_{\max}]$

22: Go back to step 11.

23: **end if**

24: Draw: $\log \lambda \mid \log \lambda^{(t-1)} \sim \mathcal{N}(\log \lambda^{(t-1)}, s_2)$

25: Compute: $\mathbf{u}' = R_\lambda \zeta^{(t)}$

26: Compute: $\alpha_\lambda = \min \left\{ 1, \frac{\mathcal{N}(\mathbf{y} \mid 0, A Q_{\mathbf{u}'}^{-1} A^T + \sigma_\varepsilon^{2(t)} I_m) \pi(\log \lambda)}{\mathcal{N}(\mathbf{y} \mid 0, A Q_{\mathbf{u}'}^{-1} A^T + \sigma_\varepsilon^{2(t)} I_m) \pi(\log \lambda^{(t-1)})} \right\}$

27: With probability α_λ set $\log \lambda^{(t)} = \log \lambda$ and $\mathbf{u} = \mathbf{u}'$, otherwise set $\log \lambda^{(t)} = \log \lambda^{(t-1)}$

28: **end for**

5 Experiments

We apply the sparse non-stationary hierarchical methodology to simulated one-dimensional interpolation experiments (Figure 2) and to a cosmic noise time-series example in Section 5.2. The experiments study the effects of the discretisation and sample size on the efficiency of the algorithms and accuracy of the estimates for the different sampling methodologies.

5.1 Simulated Data

We consider two simulated datasets with different characteristics. The first example (Figure 2a) is a function which has smooth parts and edges, and it is also piecewise constant,

$$z(x) = \begin{cases} \exp\left(4 - \frac{25}{x(5-x)}\right) & x \in (0, 5) \\ 1 & x \in [7, 8] \\ -1 & x \in (8, 9) \\ 0 & \text{otherwise} \end{cases}.$$

The second (Figure 2b) corresponds to a damped sine wave function,

$$z(x) = \exp(-x) \cos(2\pi x).$$

In the first simulated dataset, we investigate, empirically, posterior consistency of the estimates

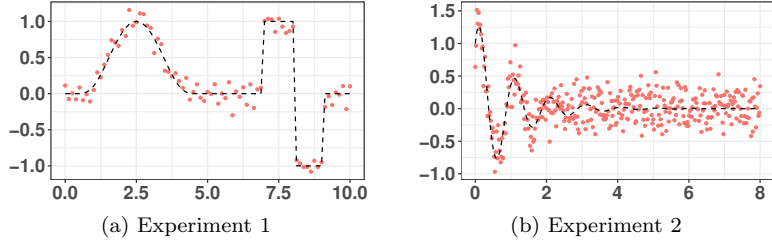


Figure 2: Simulated dataset. (a): 81 observations with domain $[0, 10]$ and noise variance $\sigma_\varepsilon^2 = 0.01$. (b): 350 observations with domain $[0, 8]$ and noise variance $\sigma_\varepsilon^2 = 0.04$.

with respect to the discretisation scheme. The second experiment explores the performance of the sampling schemes as we increase the sample size and measurement noise. In both experiments, we assign broad priors for the noise variance and length-scale hyperparameter.

Experiment 1: Smooth-piecewise constant function

For all experiments, we use the same initialization and run the chains for $T = 350,000$ iterations with a burn-in period of 100,000. Numerical discretisation-invariance is studied by varying n in the experiments, with $n = 81, 161, 241$.

We start by presenting the results obtained with the MWG algorithm. Figure 3 shows estimates of the spatially varying length-scales and the unknown function when using the AR(1) hyperprior. Inspection of traceplots and cumulative averages of the estimates (not shown) suggest convergence

of the chains. In addition, the varying length-scale estimate exhibit the expected behaviour, and the interpolated estimates indicate a reasonable fit to the unknown function for all three discretisations schemes. Figure 4 illustrates the results obtained with SE hyperprior for the same

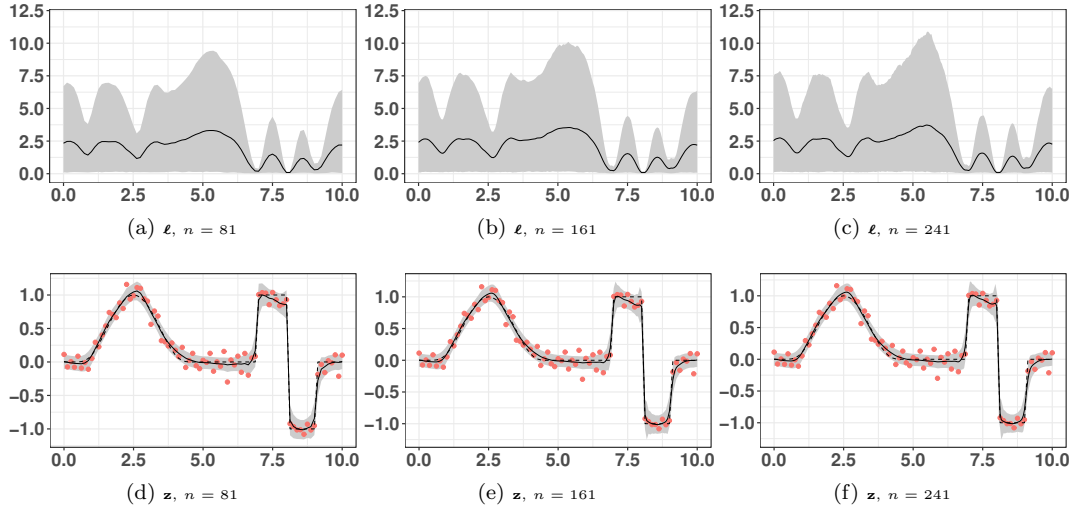


Figure 3: Results for AR(1) hyperprior with the MWG algorithm on different grids with 81 measurements. (a)-(c): Estimated ℓ process with 95% credible intervals. (d)-(f): Estimated \mathbf{z} process with 95% credible intervals.

sampling algorithm. Under this setting, the effect of discretisation scheme is evident. As we increase n , the method fails to recover the unknown function. The strong correlation between the elements of \mathbf{u} induced by the SE hyperprior makes the algorithm converge rather slowly to the target distribution.

Figure 5 depicts the results obtained with w-ELL-SS and AR(1) hyperprior. Despite the fact that chains of the hyperparameter show slower mixing compared to those corresponding to MWG (see Table 4), the estimates of ℓ and \mathbf{z} look as expected. In contrast to the results obtained for SE hyperprior with MWG, the w-ELL-SS scheme for this hyperprior demonstrates good performance as can be seen from Figure 6.

Figure 7 and 8 display the results obtained with m-ELL-SS sampling. The estimated length-scales, for both hyperpriors, appear smoother compared to those obtained with w-ELL-SS. However, the posterior estimates of the unknown function resemble each other.

To visually asses the mixing of the chains, we show traceplots and plots of cumulative averages for some of the estimates in Figure 9. The results are shown for the most challenging scenario, SE hypermodel at the highest resolution, $n = 241$. The results emphasize the lack of convergence for the MWG sampler, and the high autocorrelation of the chains produced by w-ELL-SS.

To summarise the results and to facilitate comparison, we present, in Table 1, posterior mean estimates for some of the parameters using the three different MCMC algorithms with both hyperpriors and under different discretisations schemes. With exception of the results obtained with MWG for SE hyperprior, the estimates appear consistent for the three sampling methodologies and for the three different discretisation schemes. The table also reports mean absolute error (MAE)

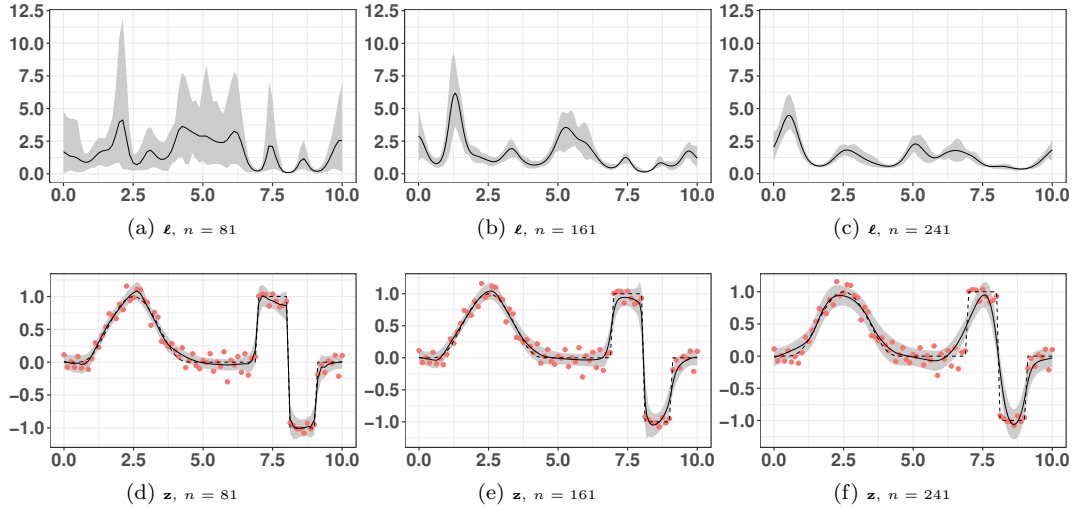


Figure 4: Results for SE hyperprior with the MWG algorithm on different grids with 81 measurements. (a)-(c): Estimated ℓ process with 95% credible intervals. (d)-(f): Estimated z process with 95% credible intervals.

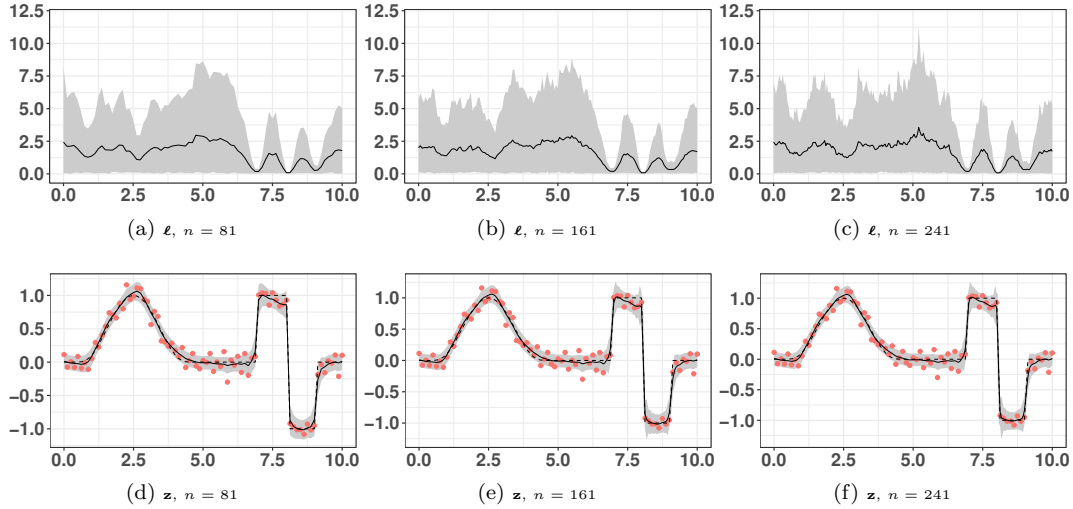


Figure 5: Results for AR(1) hyperprior with the w-ELL-SS algorithm on different grids with 81 measurements. (a)-(c): Estimated ℓ process with 95% credible intervals. (d)-(f): Estimated z process with 95% credible intervals.

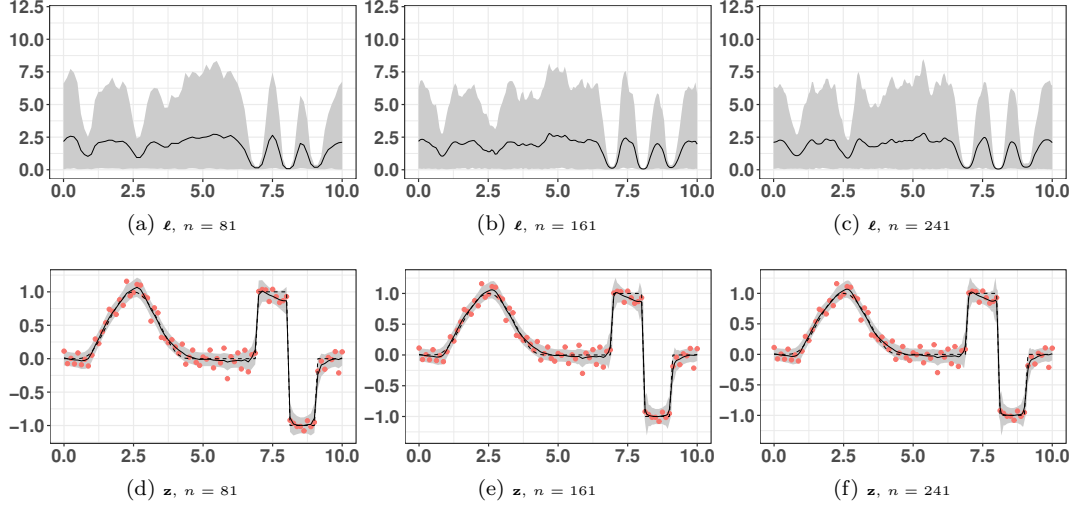


Figure 6: Results for SE hyperprior with the w-ELL-SS algorithm on different grids with 81 measurements. (a)-(c): Estimated ℓ process with 95% credible intervals. (d)-(f): Estimated z process with 95% credible intervals.

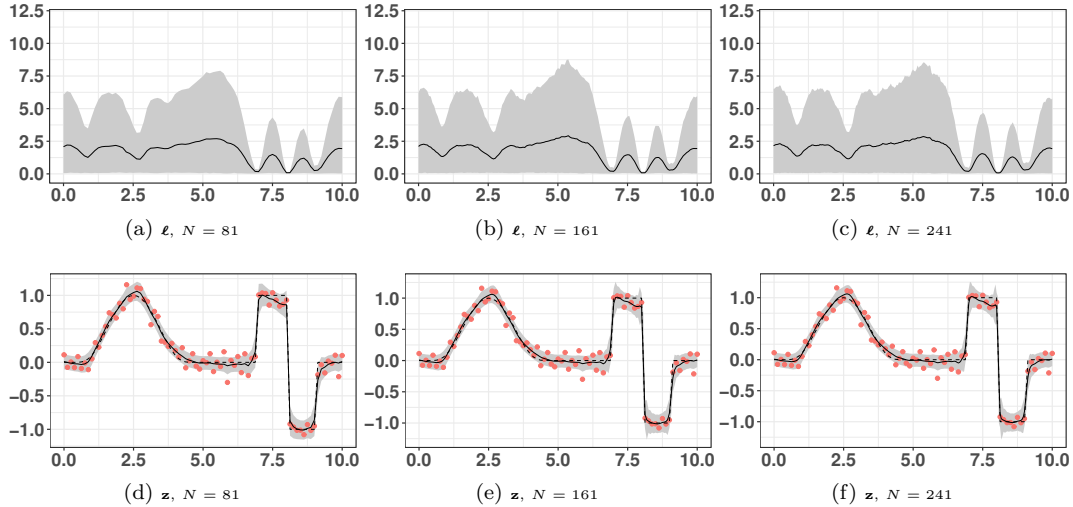


Figure 7: Results for AR(1) hyperprior with the m-ELL-SS algorithm on different grids with 81 measurements. (a)-(c): Estimated ℓ process with 95% credible intervals. (d)-(f): Estimated z process with 95% credible intervals.

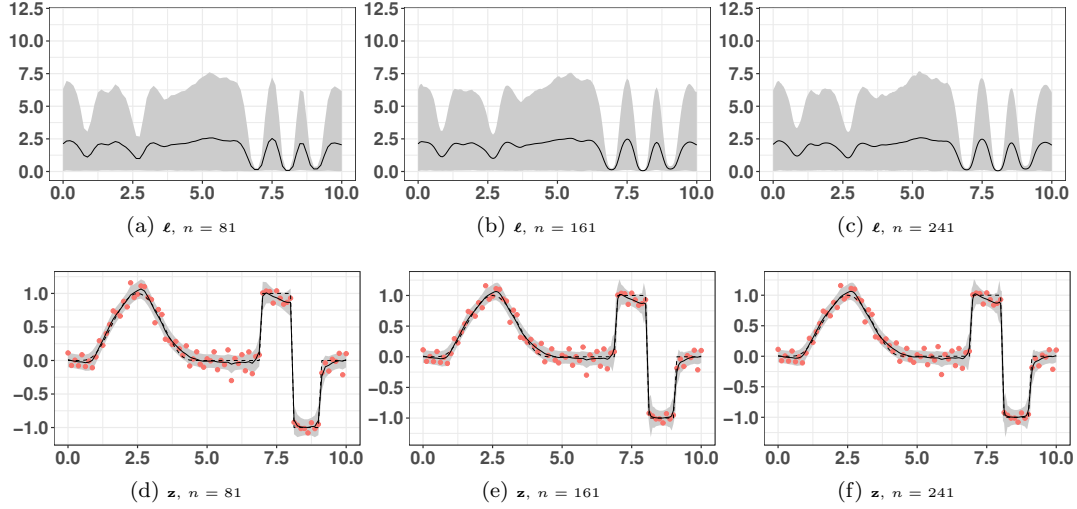


Figure 8: Results for SE hyperprior model with m-ELL-SS algorithm on different grids with 81 measurements. (a)-(c): Estimated ℓ process with 95% credible intervals. (d)-(f): Estimated z process with 95% credible intervals.

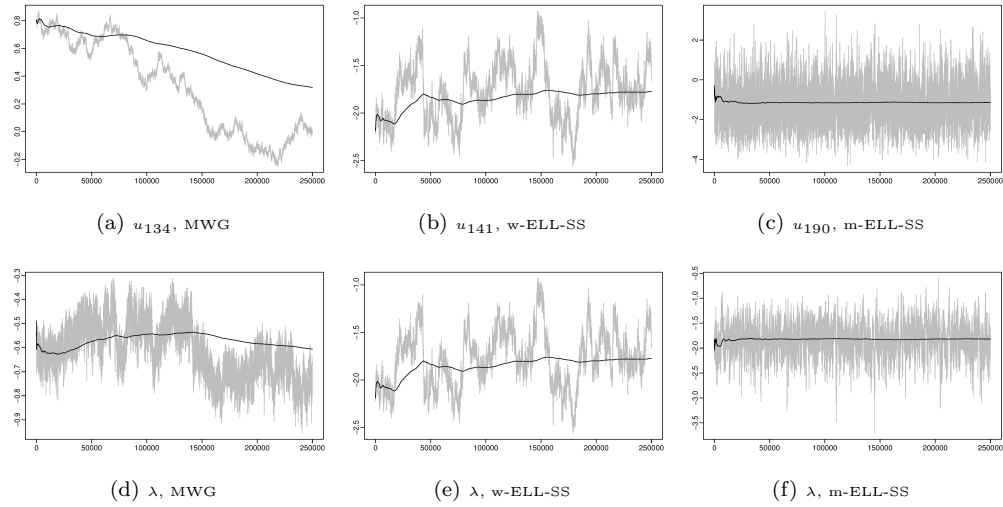


Figure 9: Traceplots with cumulative averages of the chains for SE hypermodel and $n = 241$. (Top row:) shows the element of u with the lowest ESS. (Bottom row:) illustrates the hyperparameter.

to evaluate the fit to the unknown function. While w-ELL-SS and m-ELL-SS report equivalent errors, MWG yields larger values, which is more evident for SE hypermodel.

	MWG			w-ELL-SS			m-ELL-SS		
	$n = 81$	$n = 161$	$n = 241$	$n = 81$	$n = 161$	$n = 241$	$n = 81$	$n = 161$	$n = 241$
AR(1)	σ_ε^2	0.014	0.015	0.015	0.014	0.014	0.014	0.014	0.014
	ℓ_j	2.455	2.658	2.696	1.817	1.910	2.323	2.144	2.238
	ℓ_i	0.092	0.091	0.094	0.088	0.081	0.101	0.089	0.089
	z_j	0.687	0.686	0.687	0.695	0.695	0.693	0.692	0.693
	z_i	-0.872	-0.860	-0.851	-0.873	-0.865	-0.860	-0.877	-0.866
	λ	0.391	0.370	0.365	0.359	0.371	0.316	0.355	0.345
MAE		0.041	0.051	0.054	0.041	0.050	0.053	0.041	0.050
SE	σ_ε^2	0.014	0.021	0.046	0.013	0.013	0.013	0.013	0.013
	ℓ_j	2.183	2.136	0.617	2.261	2.103	2.083	2.169	2.125
	ℓ_i	0.089	0.148	0.570	0.083	0.076	0.074	0.083	0.076
	z_j	0.678	0.669	0.711	0.692	0.695	0.693	0.693	0.693
	z_i	-0.859	-0.677	-0.234	-0.882	-0.881	-0.873	-0.887	-0.876
	λ	0.276	0.377	0.549	0.192	0.163	0.177	0.181	0.174
MAE		0.044	0.065	0.108	0.039	0.049	0.052	0.039	0.049

Table 1: Posterior mean estimates obtained with both hyperpriors under various discretisation schemes ($n = 81, 161, 241$) and employing three different sampling algorithms. $j = 15, 29, 43$ and $i = 66, 131, 196$. Lowest values of MAE are in boldface.

In order to evaluate the performance of the algorithms previously discussed, we show in Table 2 an overall efficiency score (*OES*) of the chains (Titsias and Papaspiliopoulos, 2016). This measure considers both the CPU time (Table 3) required to run the chains and the effective sample size (*ESS*) (Table 4). The score is computed as $OES = ESS/CPUtime^1$. For both multidimensional vectors, \mathbf{z} and \mathbf{u} , we report the *OES* computed with the minimum *ESS* across all dimensions. The results indicate that while MWG with the AR(1) hyperprior shows the highest efficiency score

	MWG			w-ELL-SS			m-ELL-SS		
	$n = 81$	$n = 161$	$n = 241$	$n = 81$	$n = 161$	$n = 241$	$n = 81$	$n = 161$	$n = 241$
AR(1)	σ_ε^2	264.35	32.44	7.37	175.98	36.78	12.97	190.84	51.02
	ℓ_{min}	126.88	10.18	1.89	3.53	0.95	0.24	46.33	10.38
	z_{min}	247.29	23.84	4.28	19.19	3.76	0.53	89.68	21.60
	λ	37.50	3.10	0.49	10.34	1.57	0.66	35.10	10.27
SE	σ_ε^2	213.59	2.15	8.31	233.04	50.09	13.03	293.51	62.32
	ℓ_{min}	0.12	0.01	0.00	4.05	0.51	0.23	34.79	6.69
	z	7.53	0.37	0.40	16.35	2.71	1.52	97.98	24.86
	λ	0.66	0.34	0.09	1.21	0.11	0.06	4.64	1.34
<i>OES</i>		24.34	2.29	11.62	0.58				

Table 2: OES with both hyperpriors under various discretisation schemes ($n = 81, 161, 241$) and employing three different sampling algorithms. ℓ_{min} and z_{min} report OES for the minimum ESS across all dimensions. Highest values in boldface.

for $n = 81$, its performance deteriorates as n increases. This suggests that this sampling scheme will not perform efficiently for bigger datasets even when $m = n$ (this is explored in Example 2). Notice also that the scores reported for MWG with the SE hyperprior are not informative as the chains show convergence problems. Furthermore, despite the fact that w-ELL-SS algorithm reports the lowest CPU time under both hyperpriors (Table 3), its overall efficiency scores are outperformed by those obtained with m-ELL-SS; this is due to the low autocorrelation of the chains achieved by the marginal sampler (see Table 4).

¹All experiments were run in an Intel(R) Core(TM) i7-6700 CPU 3.40GHz computer with 16 GB of RAM.

		$n = 81$	$n = 161$	$n = 241$
AR(1)	MWG	52.5	275.4	863.5
	w-ELL-SS	40.4	186.3	551.3
	m-ELL-SS	78.9	309.4	880.8
SE	MWG	58.2	278.8	1064.6
	w-ELL-SS	48.7	236.3	705.5
	m-ELL-SS	76.5	333.9	834.0

Table 3: CPU time in minutes. Best values in boldface

		MWG			w-ELL-SS			m-ELL-SS		
		$n = 81$	$n = 161$	$n = 241$	$n = 81$	$n = 161$	$n = 241$	$n = 81$	$n = 161$	$n = 241$
AR(1)	σ_ε^2	13890.2	8933.1	6365.7	7109.9	6852.3	7152.3	15049.5	15788.9	14790.5
	ℓ_{15}	8786.9	3189.6	2232.3	278.7	260.6	207.9	4744.6	4730.1	4722.4
	ℓ_{66}	32143.5	12276.5	9713.9	948.7	445.3	180.5	11920.7	3598.4	4113.9
	z_{15}	34418.4	16863.7	10777.0	6496.6	6689.2	7657.3	37441.9	42531.4	43879.4
	z_{66}	52438.7	40785.7	28194.4	10055.0	7942.6	6602.0	34297.7	33835.5	36876.1
	λ	1970.4	854.4	423.6	417.7	292.9	365.4	2768.0	3178.6	3216.4
SE	σ_ε^2	12433.9	599.0	8847.2	11358.6	11835.9	9191.8	22455.3	20811.9	20296.1
	ℓ_{15}	28.8	6.1	9.8	302.4	336.4	314.4	4340.7	4952.4	4781.2
	ℓ_{66}	49.7	4.2	2.5	1099.8	791.5	881.2	12194.1	11043.5	11023.2
	z_{15}	10082.2	91521.7	79699.1	4466.5	5969.3	5007.5	33461.0	36047.8	36027.8
	z_{66}	12382.3	102.7	10660.5	15755.4	13895.1	18866.0	39636.5	62387.3	57307.5
	λ	38.4	95.8	97.0	59.2	26.2	44.9	355.0	446.2	481.5

Table 4: ESS after burn-in period for both hyperpriors under various discretisation schemes ($n = 81, 161, 241$) and employing three different sampling algorithms. Highest values in boldface.

Experiment 2: Damped sine wave

This example explores the effect of increasing the sample size and measurement noise. Due to robustness of the estimates with respect to the discretisation in the first example, we only present experiments for the discretisation scheme when $m = n$. For these experiments, we run the chains for $T = 150,000$ iterations and apply a burn-in period of 50,000.

Figures 10 and 11 illustrate posterior estimates for the length-scales and the unknown function under AR(1) and SE hyperpriors, respectively. While the results with the AR(1) hyperprior appear satisfactory under the three sampling schemes, the SE hyperprior with MWG is not able to explore the posterior of \mathbf{u} , resulting in poor estimates and the highest MAE (see Table 5). There is a boundary effect in the estimator, i.e. the estimator shows a rise, even though it should be flat line. This is due to the boundary perturbation of the prior formed via the SPDE formulation in (8). Here our emphasis is on interpolation and not prediction at the boundary or outside the domain. However, in applications where this is relevant, one can utilise boundary correction terms, periodic boundary conditions or extension of the domain (Roininen et al., 2014).

An analysis of the efficiency of the sampling methodologies reveals that, while w-ELL-SS is consistently faster (Table 6), the ESS of its chains is consistently smaller, hence reducing the overall efficiency score (shown in Table 8).

In contrast, despite the fact that the marginal sampler reports larger CPU times, the low correlation of its chains (Table 7) favors its OES. This, together with the negligible differences in MAE, suggests that m-ELL-SS offers a good compromise between computational cost and efficiency.

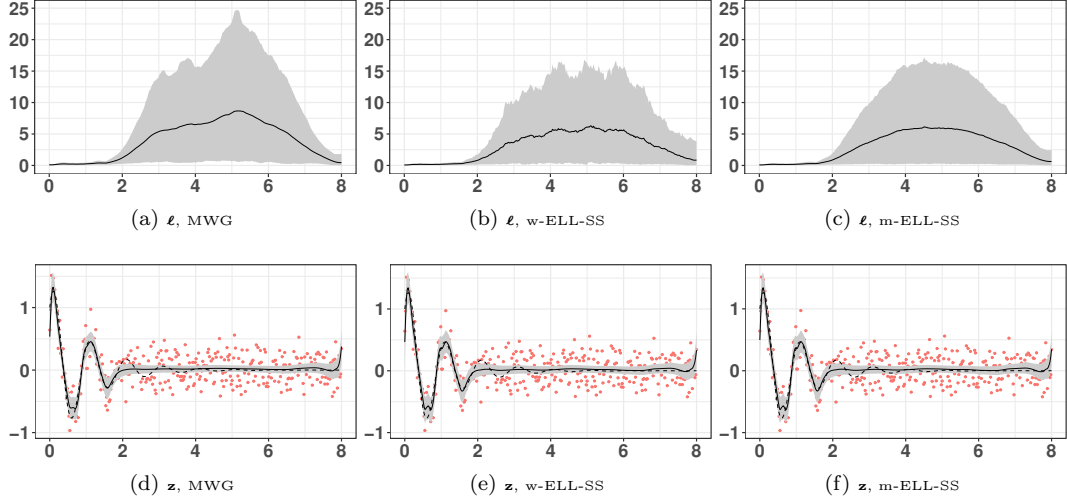


Figure 10: Results for the AR(1) hyperprior. Top row: estimated ℓ process with 95% credible interval for (a) MWG, (b) w-ELL-SS and (c) m-ELL-SS. Bottom row: estimated z process with 95% credible interval for (a) MWG, (b) w-ELL-SS and (c) m-ELL-SS.

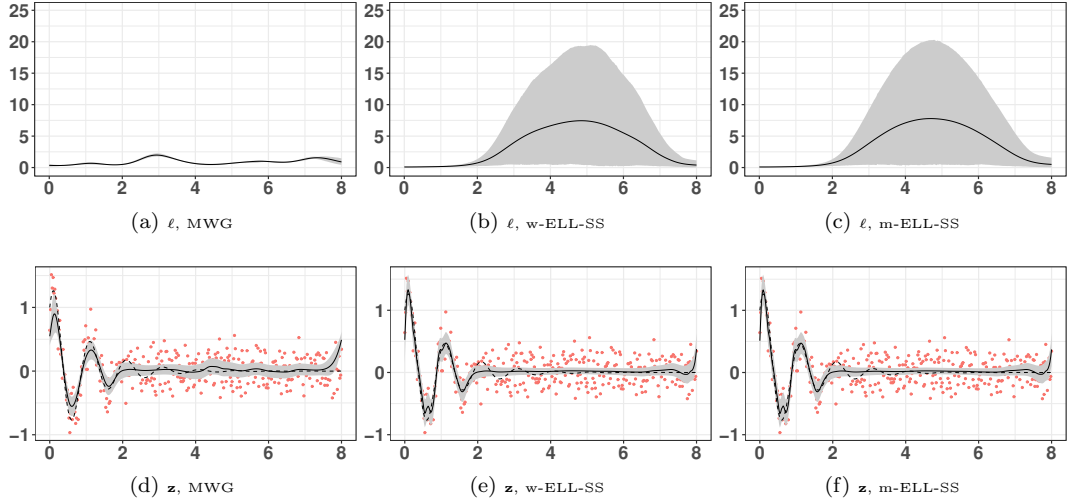


Figure 11: Results for the SE hyperprior. Top row: estimated ℓ process with 95% credible interval for (a) MWG, (b) w-ELL-SS and (c) m-ELL-SS. Bottom row: estimated z process with 95% credible interval for (a) MWG, (b) w-ELL-SS and (c) m-ELL-SS.

		MWG	w-ELL-SS	m-ELL-SS
AR(1)	σ_ε^2	0.045	0.044	0.044
	ℓ_{100}	2.266	1.428	1.599
	ℓ_{200}	7.270	5.323	6.060
	z_{100}	0.017	0.049	0.024
	z_{200}	0.027	0.062	0.031
	λ	1.354	1.533	1.461
MAE		0.043	0.044	0.044
SE	σ_ε^2	0.054	0.044	0.044
	ℓ_{100}	0.815	1.275	1.250
	ℓ_{200}	0.501	7.337	7.763
	z_{100}	0.026	0.062	0.024
	z_{200}	0.069	0.052	0.026
	λ	0.666	1.177	1.232
MAE		0.065	0.045	0.045

Table 5: Posterior mean estimates obtained with both hyperpriors and employing three different sampling algorithms. Lowest values of MAE are in boldface.

	MWG	w-ELL-SS	m-ELL-SS
AR(1)	1208.2	752.3	1955.6
SE	1491.2	712.1	1875.8

Table 6: CPU time in minutes

	MWG	w-ELL-SS	m-ELL-SS	
AR(1)	σ_ε^2	15380.2	20718.6	27788.0
	ℓ_{100}	230.3	284.4	2624.6
	ℓ_{200}	180.8	229.8	2783.6
	z_{100}	5675.4	11546.2	35876.0
	z_{200}	9219.5	5993.3	27695.3
	λ	225.1	272.5	1854.739
SE	σ_ε^2	396.1	22992.1	28635.3
	ℓ_{100}	2.4	703.2	5798.8
	ℓ_{200}	1.8	560.6	3203.9
	z_{100}	129526.3	16839.0	71063.6
	z_{200}	130973.1	6279.0	26194.2
	λ	33.9	33.8	465.1

Table 7: ESS after burnin period for both hyperprior and employing three different sampling algorithms. Highest values in boldface.

		MWG	w-ELL-SS	m-ELL-SS
AR(1)	σ_ε^2	12.73	27.54	14.21
	ℓ_{min}	0.06	0.14	0.65
	z_{min}	0.13	0.13	0.75
	λ	0.19	0.36	0.95
SE	σ_ε^2	0.27	32.29	15.27
	ℓ_{min}	0.00	0.40	1.04
	z_{min}	0.01	0.55	1.41
	λ	0.02	0.05	0.25

Table 8: OES with AR(1) and SE hyperprior employing three different sampling algorithms. ℓ_{min} and z_{min} report OES for the minimum ESS across all dimensions. Highest values in boldface.

5.2 Real data: Riometer cosmic noise time-series

We consider riometer (Relative Ionospheric Opacity Meter for Extra-Terrestrial Emissions of Radio noise) data from the Kilpisjärvi Atmospheric Imaging Receiver Array (KAIRA) instrument operated by the Sodankylä Geophysical Observatory of the University of Oulu, Finland (McKay-Bukowski et al., 2015). KAIRA measures the power of radio emissions from the sky at given frequencies and directions. The radio waves are attenuated in ionospheric plasma (at altitudes around 50–100 km) during ionization events, such as solar-flare induced photoionization. Here, as a simple example, we have a 500-second riometer dataset measured 32 MHz radiofrequency, and the objective is to deduce the background signal of this noisy measurement sampled at 1 Hz.

We employ the m-ELL-SS algorithm to do inference. Figure 12 illustrates the results. Under both hyperpriors, the model is able to capture non-stationarities through the spatially varying length-scale, with posterior estimates suggesting a decay in the correlation of the unknown signal around observation 250, in accordance with the observed measurements. Although posterior mean estimates of the unknown signal for both hyperpriors look similar, the estimated length-scale process appears smoother under SE hypermodel. Similar to second synthetic test case, here we have boundary perturbations, but as our actual goal is in analysing the non-stationarities in the middle of the signal, we can neglect boundaries of the estimates.

	AR(1)	SE
σ_ε^2	0.051	0.051
ℓ_{250}	16.441	10.563
ℓ_{400}	42.431	49.071
z_{250}	0.179	0.202
z_{400}	0.969	0.969
λ	87.265	50.224

Table 9: Posterior mean estimates for Riometer data.

6 Discussion

We presented non-stationary hierarchical models based on stochastic parameters and Gaussian Markov random fields, where we incorporate inference of the noise variance and hyperparameters of the model. This representation ameliorates the computational constraints of doing exact inference in 2-level GP models. This gain is introduced to the model through sparsity in the finite-dimensional approximation of the inverse covariance matrix of the non-stationary field.

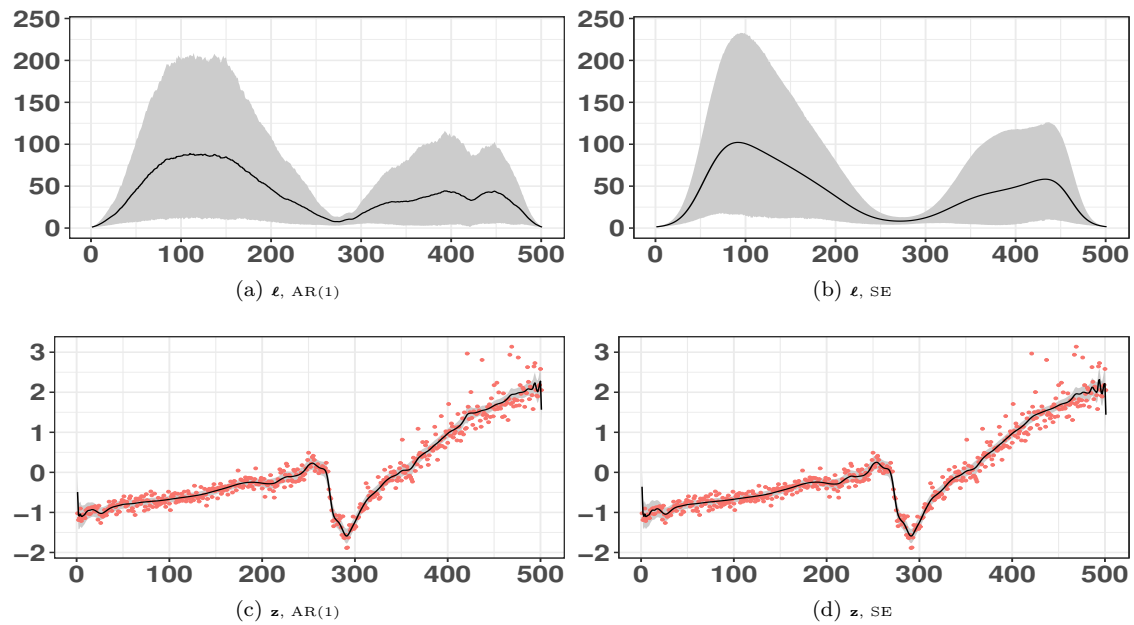


Figure 12: Results for Riometer data. Top row: estimated ℓ process with 95% credible interval for (a) m-ELL-SS with AR(1) hyperprior and (b) m-ELL-SS with SE hyperprior. Bottom row: estimated z process with 95% credible interval for (c) m-ELL-SS with AR(1) hyperprior and (d) m-ELL-SS with SE hyperprior.

We explored different hyperpriors for the spatially varying length-scale. On the one hand, we introduce strong prior smoothness assumptions by using a squared exponential covariance function. On the other hand, we explore rough hyperpriors, thorough an autoregressive AR(1) model. The latter representation adds further computational gains to the model under certain sampling schemes, when evaluation of the precision matrix, not the covariance matrix, is required, e.g. MWG.

We also introduce and investigate the performance of three different MCMC algorithms. First, we proposed a Metropolis-within-Gibbs (MWG) scheme, which we found to perform poorly for highly correlated hyperpriors and to exhibit deteriorating effectiveness as the number of observations increases. The second corresponds to a whitened elliptical slice sampling (w-ELL-SS), which performs well regardless the hyperprior employed with low computational time at the price of highly correlated chains. Finally, we consider a marginal elliptical slice sampler with whitening (m-ELL-SS), which appears to be an efficient strategy to break the correlation between latent process and hyperparameters and offers a good compromise between computational complexity, scalability and efficiency of the chains.

The experiments here presented suggest that the algorithms based on elliptical slice sampling do not appear to deteriorate as the resolution becomes finer or as we increase the sample size, similar to the schemes discussed by [Chen et al. \(2018\)](#). However, it is important to emphasize that elliptical slice sampling is known to perform well for weak data likelihoods; therefore, care must be taken in the small noise limit. Furthermore, it will be interesting to explore the performance of the auxiliary gradient-based sampling scheme recently proposed by [Titsias and Papaspiliopoulos \(2016, Section 4\)](#), which appears as a promising alternative to the algorithms presented here. However, notice that these schemes require derivatives, which are not straightforward to compute for our model and will bring in extra computational cost. Alternatively to MCMC methods, we aim to investigate the performance of variational Bayes techniques to approximate the posterior of interest.

A natural extension of this work is to extend the proposed algorithms for efficient inference with the 3-level Gaussian process model or, more generally, the deep Gaussian process models studied in [Dunlop et al. \(2017\)](#). Other interesting directions for future research include exploring higher-order autoregressive hyperpriors and extending the methodology for multivariate inputs; more general kernel matrices; and alternative likelihoods for problems beyond regression, such as the classification and inverse problems discussed in [Chen et al. \(2018\)](#).

References

Ethan B Anderes and Michael L Stein. Estimating deformations of isotropic Gaussian random fields on the plane. *The Annals of Statistics*, pages 719–741, 2008. [1](#)

Veronica J Berrocal, Adrian E Raftery, Tilmann Gneiting, and Richard C Steed. Probabilistic weather forecasting for winter road maintenance. *Journal of the American Statistical Association*, 105(490):522–537, 2010. [1](#)

Victor Chen, Matthew M Dunlop, Omiros Papaspiliopoulos, and Andrew M Stuart. Robust mcmc sampling with non-gaussian and hierarchical priors in high dimensions. *arXiv preprint arXiv:1803.03344*, 2018. [24](#)

Matthew M Dunlop, Mark Girolami, Andrew M Stuart, and Aretha L Teckentrup. How deep are deep gaussian processes? *arXiv preprint arXiv:1711.11280*, 2017. [24](#)

Maurizio Filippone, Mingjun Zhong, and Mark Girolami. A comparative evaluation of stochastic-based inference methods for Gaussian process models. *Machine Learning*, 93(1):93–114, 2013. [10](#)

Francky Fouedjio, Nicolas Desassis, and Jacques Rivoirard. A generalized convolution model and estimation for non-stationary random functions. *Spatial Statistics*, 16:35–52, 2016. [1](#)

Geir Arne Fuglstad, Finn Lindgren, Daniel Simpson, and Håvard Rue. Exploring a new class of non-stationary spatial gaussian random fields with varying local anisotropy. *Statistica Sinica*, pages 115–133, 2015a. [2](#)

Geir Arne Fuglstad, Daniel Simpson, Finn Lindgren, and Håvard Rue. Does non-stationary spatial data always require non-stationary random fields? *Spatial Statistics*, 14:505–531, 2015b. [2](#)

Robert B Gramacy and Herbert KH Lee. Bayesian treed gaussian process models with an application to computer modeling. *Journal of the American Statistical Association*, 2012. [1](#)

Markus Heinonen, Henrik Mannerström, Juho Rousu, Samuel Kaski, and Harri Lähdesmäki. Non-stationary gaussian process regression with hamiltonian monte carlo. In *Artificial Intelligence and Statistics*, pages 732–740, 2016. [4](#)

Jari Kaipio and Erkki Somersalo. *Statistical and computational inverse problems*, volume 160. Springer Science & Business Media, 2006. [1](#)

Hyoung-Moon Kim, Bani K Mallick, and CC Holmes. Analyzing nonstationary spatial data using piecewise gaussian processes. *Journal of the American Statistical Association*, 100(470):653–668, 2005. [1](#)

Tobias Lang, Christian Plagemann, and Wolfram Burgard. Adaptive non-stationary kernel regression for terrain modeling. In *Robotics: Science and Systems*, 2007. [4](#)

Finn Lindgren, Hvard Rue, and Johan Lindström. An explicit link between Gaussian fields and Gaussian Markov random fields: the stochastic partial differential equation approach. *Journal of the Royal Statistical Society - Series B*, 73(4):423–498, 9 2011. [2](#), [4](#), [5](#)

Georges Matheron. The intrinsic random functions and their applications. *Advances in Applied Probability*, pages 439–468, 1973. [1](#)

D. McKay-Bukowski, J. Vierinen, I. I. Virtanen, R. Fallows, M. Postila, T. Ulich, O. Wucknitz, M. Brentjens, N. Ebbendorf, C. F. Enell, M. Gerbers, T. Grit, P. Gruppen, A. Kero, T. Iinatti, M. Lehtinen, H. Meulman, M. Norden, M. Orispää, T. Raita, J. P. de Reijer, L. Roininen, A. Schoenmakers, K. Stuurwold, and E. Turunen. Kaira: The kilpisjärvi atmospheric imaging receiver array: System overview and first results. *IEEE Transactions on Geoscience and Remote Sensing*, 53(3):1440–1451, March 2015. ISSN 0196-2892. [22](#)

Iain Murray and Ryan P Adams. Slice sampling covariance hyperparameters of latent gaussian models. In *Advances in Neural Information Processing Systems*, pages 1732–1740, 2010. [10](#)

Iain Murray, Ryan Prescott Adams, and David JC MacKay. Elliptical slice sampling. In *AISTATS*, volume 13, pages 541–548, 2010. [8](#), [10](#)

Mari Myllymäki, Aila Särkkä, and Aki Vehtari. Hierarchical second-order analysis of replicated spatial point patterns with non-spatial covariates. *Spatial Statistics*, 8:104–121, 2014. [1](#)

Joaquim Henriques Vianna Neto, Alexandra M Schmidt, and Peter Guttorp. Accounting for spatially varying directional effects in spatial covariance structures. *Journal of the Royal Statistical Society: Series C (Applied Statistics)*, 63(1):103–122, 2014. [1](#), [2](#), [4](#)

Christopher J Paciorek and Mark J Schervish. Spatial modelling using a new class of nonstationary covariance functions. *Environmetrics*, 17(5):483–506, 2006. [2](#), [3](#), [4](#)

Mark D Risser. Nonstationary spatial modeling, with emphasis on process convolution and covariate-driven approaches. *arXiv preprint arXiv:1610.02447*, 2016. [4](#)

Gareth O. Roberts and Jeffrey S. Rosenthal. Examples of adaptive mcmc. *Journal of Computational and Graphical Statistics*, 18(2):349–367, 2009. [8](#)

Lassi Roininen, Janne MJ Huttunen, and Sari Lasanen. Whittle-matérn priors for bayesian statistical inversion with applications in electrical impedance tomography. *Inverse Problems and Imaging*, 8(2):561–586, 2014. [4](#), [19](#)

Lassi Roininen, Mark Girolami, Sari Lasanen, and Markku Markkanen. Hyperpriors for matérn fields with applications in bayesian inversion. *arXiv preprint arXiv:1612.02989*, 2016. [2](#), [4](#), [5](#), [7](#), [8](#)

P D Sampson, D Damian, and P Guttorp. Advances in modeling and inference for environmental processes with nonstationary spatial covariance. In *geoENV III — Geostatistics for Environmental Applications*, volume 11, pages 17–32. Springer, 2001. [1](#)

Vassilios Stathopoulos, Veronica Zamora-Gutierrez, Kate Jones, and Mark Girolami. Bat call identification with Gaussian process multinomial probit regression and a dynamic time warping kernel. In *Proceedings of the Seventeenth International Conference on Artificial Intelligence and Statistics*, pages 913–921, 2014. [1](#)

M.L. Stein. *Interpolation of spatial data: some theory for Kriging*. Springer Series in Statistics. Springer New York, 1999. ISBN 9781461214953. [3](#)

Michalis K Titsias and Omilos Papaspiliopoulos. Auxiliary gradient-based sampling algorithms. *arXiv preprint arXiv:1610.09641*, 2016. [18](#), [24](#)

Xiaoguang Xu, Theodore Kypraios, and Philip D O’Neill. Bayesian non-parametric inference for stochastic epidemic models using Gaussian processes. *Biostatistics*, page kxw011, 2016. [1](#)

Yaming Yu and Xiao-Li Meng. To center or not to center: That is not the question an ancillarity-sufficiency interweaving strategy (asis) for boosting mcmc efficiency. *Journal of Computational and Graphical Statistics*, 20(3):531–570, 2011. [8](#), [10](#)

Yu Ryan Yue, Daniel Simpson, Finn Lindgren, Håvard Rue, et al. Bayesian adaptive smoothing splines using stochastic differential equations. *Bayesian Analysis*, 9(2):397–424, 2014. [2](#)

Hao Zhang. Inconsistent estimation and asymptotically equal interpolations in model-based geostatistics. *Journal of the American Statistical Association*, 99(465):250–261, 2004. [6](#)

Acknowledgements

Monterrubio-Gómez is supported by the Mexican National Council of Science and Technology (CONACYT) grant no. CVU609843. Lassi Roininen has been funded by Academy of Finland (project numbers 307741 and 313709).